CHEMISTRY OF MATERIALS
Article

Chem. Mater. **2010,** *22,* 1633–1639 1633
DOI:10.1021/cm9036499

In situ Encapsulation of Pt Nanoarchitectures of Varying Morphologies in Mesoporous Compounds

Atul K. Prashar,[†] Robert P. Hodgkins,[‡,§] Jima N. Chandran,[†] P. R. Rajamohanan,[†] and R. Nandini Devi*[,†]

[†]*Catalysis Division and Magnetic Resonance Group, National Chemical Laboratory, Pune 411008, India, and* [‡]*Materials Chemistry Research Group, Department of Physical, Inorganic and Structural Chemistry, Arrhenius Laboratory, Stockholm University, SE-106 91 Stockholm, Sweden.* [§]*Present address: Johnson Matthey Technology Centre, Billingham TS23 1LB, United Kingdom.*

Received August 19, 2009. Revised Manuscript Received January 20, 2010

Nanoparticle morphology could be engineered and fine-tuned based on a novel in situ template method. Different shapes of platinum nanoparticles were obtained from very low concentrations of precursors and could be isolated exclusively inside the mesochannels of SBA-15. This was achieved by dispersing a platinum precursor in surfactant modified polymer to different extents and using these composite materials as templates for the formation of mesoporous silica. $[PtCl_6]^{2-}$ interacts with the cationic headgroup of the surfactant and facilitates the isolation of precursors within the composite template leading to the formation of nanoparticles molded by the walls of the mesochannels when calcined. When this $[PtCl_6]^{2-}$−surfactant−polymer micelle composite is aged for different durations, Pt nanoparticles of various morphologies like spheroids, nano rugby balls, and nanorods are obtained.

Introduction

Giant leaps have already been made in the synthesis of metal nano architectures with different morphologies like nanorods, spheres, discs, etc.[1−10] Yet understanding and predicting the formation of specific shape reproducibly is still a challenging prospect. This is more so in the case of fabricating nanoparticles for the purpose of catalysis where the morphology and size have immense effects on the performance of materials.[11−15] Various solution methods as well as template methods have been developed to synthesize noble metal nanoforms with specific architectures. Among these, the template method suits materials for catalysis best because it is imperative to isolate nanoparticles on supports so that unique physical and morphological properties of the nanoforms are retained with minimal leaching in harsh catalytic conditions. The advent of mesoporous silica compounds like SBA-15, MCM-41, etc.,[16−18] have started an era of research into exploiting these materials as templates as well as supports.[19−22] A number of factors viz. interpenetrating channel systems, uniform pore structure distribution, etc., come together advantageously in these materials.[23,24] Nanospheres and nanorods are the most common architectures fabricated by employing mesoporous silicas, the latter by pore filling using wet or vapor infiltration of high concentrations of noble metal precursor into the channel system, which is reduced by various means to form nanorods.[25] The former are commonly synthesized either by impregnation or grafting of the precursor salts on to the mesoporous materials.[26] In these cases, however, there is a possibility of particle agglomeration on the surface of the mesoporous material outside the templating channels because no preventive measures are taken to ensure that the metal

*Corresponding author. E-mail: nr.devi@ncl.res.in.

(1) Wiley, B.; Sun, Y.; Mayers, B.; Xia, Y. *Chem.—Eur. J.* **2005**, *11*, 454.
(2) Wiley, B. J.; Chen, Y.; McLellan, J. M.; Xiong, Y.; Li, Z.-Y.; Ginger, D.; Xia, Y. *Nano Lett.* **2007**, *7*, 1032.
(3) Kan, C. K.; Zhu, X.; Wang, G. *J. Phys. Chem. B* **2006**, *110*, 4651.
(4) Whitney, T. M.; Jiang, J. S.; Searson, P. C.; Chien, C. L. *Science* **1993**, *261*, 1316.
(5) Sau, T. K.; Murphy, C. J. *J. Am. Chem. Soc.* **2004**, *126*, 8648.
(6) Shiv Shankar, S.; Rai, A.; Ankamwar, B.; Singh, A.; Ahmad, A.; Sastry, M. *Nat. Mater.* **2004**, *3*, 482.
(7) Puntes, V. F.; Krishnan, K. M.; Alivisatos, A. P. *Science* **2001**, *291*, 2115.
(8) Sun, Y.; Xia, Y. *Science* **2002**, *298*, 2176.
(9) Yin, Y.; Rioux, R. M.; Erdonmez, C. K.; Hughes, S.; Somorjai, G. A.; Alivisatos, A. P. *Science* **2004**, *304*, 711.
(10) Pileni, M. P. *J. Phys. Chem. C* **2007**, *111*, 9019.
(11) Hamilton, J. F.; Baetzold, R. C. *Science* **1979**, *205*, 1213.
(12) Johnson, B. F. G. *Top. Catal.* **2003**, *24*, 147.
(13) Bell, A. T. *Science* **2003**, *299*, 1688.
(14) Somorjai, G. A.; Borodko, Y. G. *Catal. Lett.* **2001**, *76*, 1.
(15) Grunes, J.; Zhu, J.; Somorjai, G. A. *Chem. Commun.* **2003**, 2257.
(16) Zhao, D. Y.; Huo, Q.; Feng, J.; Chmelka, B. F.; Stucky, G. D. *J. Am. Chem. Soc.* **1998**, *120*, 6020.
(17) Zhao, D. Y.; Feng, J.; Huo, Q.; Melosh, N.; Fredrickson, H. G.; Chmelka, B. F.; Stucky, G. D. *Science* **1998**, *279*, 548.
(18) Kresge, C. T.; Leonowicz, M. E.; Roth, W. J.; Vartuli, J. C.; Beck, J. S. *Nature* **1992**, *359*, 710.
(19) Fukuoka, A.; Ichikawa, M. *Top. Catal.* **2006**, *40*, 103.
(20) Fukuoka, A.; Sakamoto, Y.; Guan, S.; Inagaki, S.; Sugimoto, N.; Fukushima, Y.; Hirahara, K.; Iijima, S.; Ichikawa, M. *J. Am. Chem. Soc.* **2001**, *123*, 3373.
(21) Liu, Z.; Sakamoto, Y.; Ohsuna, T.; Hiraga, K.; Terasaki, O.; Ko, C. H.; Shin, H. J.; Ryoo, R. *Angew. Chem., Int. Ed.* **2000**, *39*, 3107.
(22) Lee, K.-B.; Lee, S.-M.; Cheon *J. Adv. Mater.* **2001**, *13*, 517.
(23) Bronstein, L. M. *Top. Curr. Chem.* **2003**, *226*, 55.
(24) Taguchi, A.; Shüth, F. *Microporous Mesoporous Mater.* **2005**, *77*, 1.
(25) Shin, H. J.; Ryoo, R.; Liu, Z.; Terasaki, O. *J. Am. Chem. Soc.* **2001**, *123*, 1246.
(26) Zhang, Z.; Dai, S.; Fan, X.; Blom, D. A.; Pennycook, S. J.; Wei, Y. *J. Phys. Chem. B* **2001**, *105*, 6755.

Published on Web 02/03/2010

precursors are solely isolated within the channels. In this context, we have been striving to develop more effective methodologies not only to synthesize platinum nanoparticles exclusively inside mesochannels but also to have an efficient control on their size and morphology. This has been achieved by dispersing very low concentrations of metal ions within template polymer micelles modified with ionic surfactants whereby the hydrophobic tail groups penetrate the micelle core and the charged head groups decorate the interface between the hydrophobic core and the hydrophilic corona. Added to this polymer−surfactant composite, metal ions interact with the surfactant head groups depending on various factors viz. aging time, surfactant and precursor concentration, etc. Calcination of this material leads to metal nanoparticles encapsulated within the mesochannels.[27]

The intent here was to identify synthetic parameters that could affect the nanoarchitecture growth and hence could easily be varied in situ. The duration for which the metal salt was kept in contact with the surfactant modified polymer micelle was found to be one parameter that controls the distribution of platinum. Hence, the metal salt was dispersed in the polymer−surfactant micelle composite for different durations prior to the addition of silica source, with the aim of producing different local concentrations. This was found to have a direct bearing on the morphology of the resulting nano form of the metal incorporated in the final mesoporous silica compounds.

Experimental Section

Synthesis. Typically, 0.0364 g of cetyltrimethylammonium bromide (CTAB, LobaChemie) was added to 100 g of 1 wt % solution of triblock copolymer polyethyleneoxide-polypropyleneoxide-polyethyleneoxide (Pluronic P123, Aldrich) so that the final composition was 1 mM of CTAB and this mixture was stirred for 12 h at 25 °C; 2.4 mL of 1% solution of H_2PtCl_6 (Aldrich) was added to this polymer−surfactant composite solution and stirred for another 15 min (**S1**), 4 h (**S2**), and 8 h (**S3**) at 40 °C. This solution was made acidic (pH < 2) by 6.25 mL conc. HCl (37%) and then 2.08 g tetraethylorthosilicate (TEOS; Aldrich) was added under stirring. This solution was heated to 40 °C under stirring for 24 h and autoclaved at 90 ± 5 °C for 48 h. The product was filtered, washed, dried, and calcined at 500 °C to enable the template removal and nanoparticle formation. The final molar composition of the gel was 1:585:6.3:0.017:0.01:0.006 TEOS:H_2O:HCl:P123:CTAB: H_2PtCl_6.

Characterization. Powder X-ray diffraction of all the samples was carried out in a PANalytical X'pert Pro dual goniometer diffractometer. A proportional counter detector was used for low angle experiments and an X'celerator solid-state detector was employed in wide-angle experiments. The radiation used was Cu Kα (1.5418 Å) with a Ni filter and the data collection was carried out using a flat holder in Bragg−Brentano geometry (0.2°/min). Care was taken to avoid sample displacement effects. Variable temperature in situ XRD experiments were carried out in an Anton-Paar XRK900 reactor under gas flow.

A JEOL JEM-3010 electron microscope operating at 300 kV (Cs = 0.6 mm, resolution 1.7 Å) was used for HRTEM sample observation. A Gatan digital camera (model 794, Gatan 1024 × 1024 pixels, pixel size 24 × 24 μm) at 15 000−80 000× magnifications was used to record micrographs. Samples were crushed and dispersed in ethanol before depositing onto a holey carbon grid. Particle size distribution was statistically analyzed from TEM images using the program ImagePro Plus.

Nitrogen adsorption/desorption isotherms were acquired using a Micromeritics ASAP 2020 instrument. The program consisting of both an adsorption and desorption branch typically ran at −196 °C after samples were degassed at 120 °C for 2 h once the final temperature had been maintained. Specific surface areas were calculated via the BET model at relative pressures of P/P_o = 0.05−0.2. The total pore volume was estimated from the uptake of adsorbate at a relative pressure of P/P_o = 0.99. Pore size distribution curves were obtained via the NLDFT model assuming cylindrical pore geometry and the micropore volume calculated via t-plot analyses as a function of relative pressure using the Broekhoff de Boer model for thickness curve individually measured for each sample (**S1**, 5.3−8.6 Å; **S2**, 3.5−7.3 Å; **S3**, 3.5−7.5 Å).

Chemical analysis was carried out in a LabTam 8440 Plasmalab sequential mode ICP-AES spectrometer. The samples were dissolved in aqua regia and the undissolved siliceous matter filtered off prior to analysis. UV−vis spectral data were acquired using a Perkin-Elmer Lambda 650 spectrometer. Ionic strengths of the solutions were normalized using KBr and the experiments were carried out in 1 mm quartz cuvettes. Variable-temperature experiments were carried out in a Praying Mantis (Harrick Scientific Inc.) accessory. IR spectra were recorded on Thermo Nicolet Nexus 870 FT-IR and Shimadzu FTIR-8300 spectrometers.

All the NMR measurements were carried out on a Bruker AV400 NMR spectrometer operating at 400 MHz for ^{1}H. at 30 °C using a 5 mm broadband observe gradient probe. All the samples were prepared in 99.98% D_2O and the chemical shifts were referred to TSP at 0 ppm. The self-diffusion measurements were conducted in the same probe at 30 °C using a standard Bruker pulse sequence incorporating longitudinal eddy current delay.[28] Data were acquired with a 50 ms diffusion delay, 2 or 1.8 ms bipolar gradient pulses, 1 ms spoil gradient pulse and 5 ms eddy current delay. The bipolar pulse gradient strength was varied incrementally from 2 to 95%. The experimentally observed diffusion coefficients were then determined by on line processing of the data using the Bruker T1/T2 analytical tool. The data were fitted to the following equation

$$I = I_0 \exp[-D(G\delta\gamma)^2(\Delta - \delta/3)]$$

Where I is the observed intensity, I_0 is the signal intensity or integral in the absence of gradient pulse, D the diffusion coefficient, γ is the gyro magnetic ratio of proton, G the magnetic gradient pulse amplitude, δ the length of the gradient pulse, and Δ the diffusion delay time.

Results and Discussion

The strategy employed in the synthetic methodology is to add low concentrations of an ionic surfactant like CTAB to non ionic block copolymer, P123 so that the interaction is cooperative whereby the hydrophobic tail of the surfactant is anchored to the core and the ionic headgroup is dispersed in the core−corona interface of the polymer

(27) Prashar, A. K.; Hodgkins, R. P.; Kumar, R.; Devi, R. N. *J. Mater. Chem.* **2008**, *18*, 1765.

(28) Gibbs, S. J.; Johnson, C. S., Jr. *J. Magn. Reson.* **1991**, *93*, 395.

micelle.[29−31] When H_2PtCl_6 is added, the electrostatic interaction directs the $[PtCl_6]^{2-}$ toward the cationic head groups and an ion exchange with the counteranions of the surfactant is possible. This type of specific surfactant-metal complex interaction has been reported earlier for Pd, Au and Ru complexes.[32−34] It is proposed that an ion pair, $(CTA^+)_xMX_n^{x-}$ exists in the premicellar form and above cmc, the ion pair is solubilized inside the surfactant micelle. In the present work, CTAB in the premicellar form is dispersed in the hydrophobic region of the polymer micelle, whereas the head groups decorate the core−corona interface. Thus, $[PtCl_6]^{2-}$, as a result of the interaction with the $R-N(CH_3)_3^+$ group is expected to be dispersed in the interface. This method has been used for the synthesis of metal nanoparticles isolated in the corona of polymer micelles after reduction of metal precursors with $NaBH_4$ etc.[35,36] However, we have utilized this $[PtCl_6]^{2-}$−surfactant−polymer micelle composite as a template for mesoporous silica formation before reduction, hence the Pt(IV) exists as complexed to the CTAB-P123 composite during silica hydrolysis and condensation around the template to form channels. Here, we assume that the metal reduction occurs during removal of the organic matter by calcination and nanoparticles form mainly by Ostwald ripening mechanism based on nutrient availability, post-synthesis of the mesoporous silica. The fact that $[PtCl_6]^{2-}$ is anchored exclusively inside the micelle composite is advantageous to ensure that the nanoparticles formed at a later stage are encapsulated by the silica walls upon mesoporous compound formation.

A microphase separation and aggregation with storage time has been reported in case of surfactant−metal complex system in the post-micelle regime.[33] Even though in our system we expect more of a premicellar ion pair formation because of CTAB dispersion in polymer, it is possible to envisage a dynamic process in which the $[CTA]_2[PtCl_6]$ complex is solubilized within the polymer micelle and an aggregation of this ion pair occurs with time. Hence, if the duration for which the $[PtCl_6]^{2-}$−surfactant−polymer micelle composite is allowed to age is varied, then it is possible to control the extent of agglomeration and metal ion distribution within the surfactant polymer composite thereby varying the local availability of nutrients for nanoparticle formation. This can lead to different nano architectures on calcination. We had earlier studied the effect of CTAB concentration on P123 and optimized it to be 2 mM before the micelle structure contracts and then collapses.[27] Hence we had used 1 mM CTAB for the formation of the micelle composite so that mesoporous material formation is not affected and 0.5 mM H_2PtCl_6 was used as platinum ion source. The H_2PtCl_6 contact time with the micelle-surfactant composite was varied from 15 min (**S1**) and 4 h (**S2**) to 8 h (**S3**). All three mesoporous compounds were characterized by XRD, N_2 adsorption, and HRTEM studies.

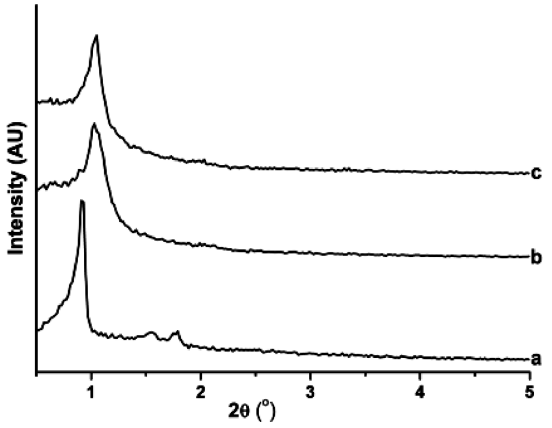

Figure 1. Low-angle PXRD patterns of Pt/SBA-15 samples with different contact times (a) 15 min, (b) 4 h, (c) 8 h. The unit-cell parameters are calculated based on hexagonal lattice; $a = \sqrt{(4/3)}d_{10}$ to be 110.8, 98.5, and 97.2 Å respectively.

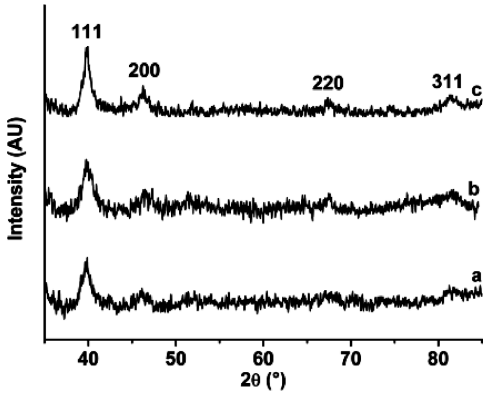

Figure 2. Wide-angle PXRD patterns of Pt/SBA-15 indicating the presence of Pt particles with increasing crystallinity; (a) 15 min, (b) 4 h, and (c) 8 h.

Powder X-ray diffraction studies of the final calcined samples show that the mesoporous nature is intact in all the three compounds. However, the long-range order is less pronounced in case of **S2** and **S3** when compared to **S1** (Figure 1). Wide-angle XRD studies indicated the presence of platinum particles and the crystallinity of platinum was enhanced with an increase in contact time as clear from the increase in intensity and the narrowing of the peaks which may be indicative of a change in size (Figure 2).

We observed a very interesting phenomenon by HRTEM. **S1** showed only spheroid nanoparticles with size in the range of 6−9 nm. As observed earlier, all the nanoparticles were isolated exclusively inside the mesochannels. The pore diameter of the mesoporous silica in this material was measured to be ~10 nm. However, the

(29) Antonietti, M.; Schmidt, M.; Rosenauer, C. *Macromolecules* **1994**, *27*, 3276.
(30) Hecht, E.; Hoffmann, H. *Langmuir* **1994**, *10*, 86.
(31) Jansson, J.; Schillen, K.; Olofsson, G.; Cardoso da Silva, R.; Loh, W. J. *J. Phys. Chem. B* **2004**, *108*, 82.
(32) Veisz, B.; Király, Z. *Langmuir* **2003**, *19*, 4817.
(33) Torigoe, K.; Esumi, K. *Langmuir* **1992**, *8*, 59.
(34) Snyder, S. W.; Buell, S. L.; Demas, J. N.; DeGraff, B. A. *J. Phys. Chem.* **1989**, *93*, 5265.
(35) Beletskaya, I. P.; Kashin, A. N.; Litvinov, A. E.; Tyurin, V. S.; Valetsky, P. M.; van Koten, G. *Organometallics* **2006**, *25*, 154.
(36) Bronstein, L. M.; Chernyshov, D. M.; Timofeeva, G. I.; Dubrovina, L. V.; Valetsky, P. M.; Obolonkova, E. S.; Khokhov, A. R. *Langmuir* **2000**, *16*, 3626.

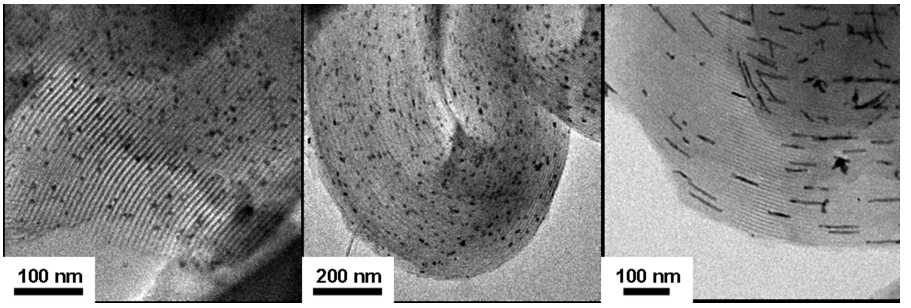

Figure 3. HRTEM images of Pt/SBA-15 synthesized with contact times of (left) 15 min, (middle) 4 h, and (right) 8 h; at short contact time, the Pt nanoparticle morphology inside the mesochannels is spheroid with an average diameter of 9 nm. As time increases, the morphology changes to rugby balls and then to nanorods.

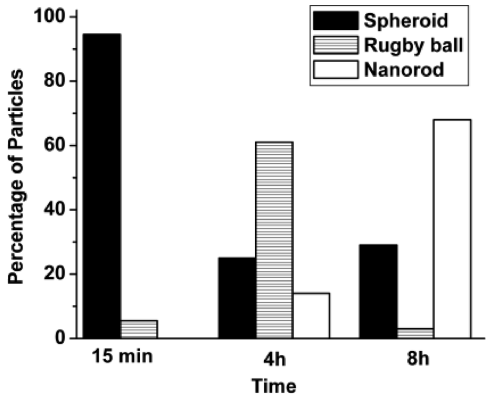

Figure 4. Particle morphology distribution of Pt/SBA-15 samples at various contact times.

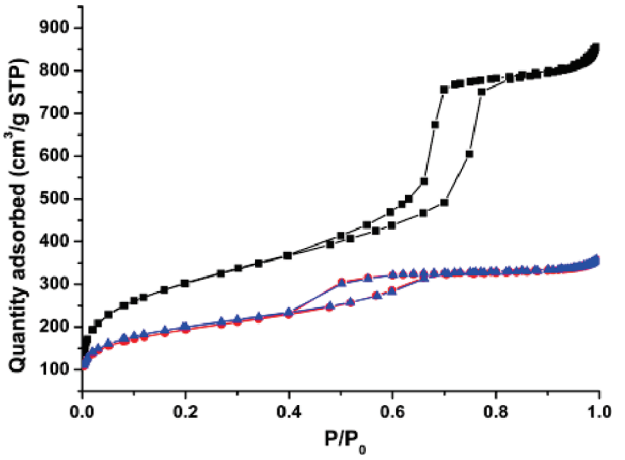

Figure 5. N_2 adsorption isotherms of samples **S1** (black), **S2** (red), and **S3** (blue).

morphology distribution changed as the contact time was increased to 4 h. A majority of the particles were more elongated rugby-ball-shaped with only a small number of spheroids, the elongation of the rugby balls being along the direction of the channels. The length of the rugby balls was in the range 13−30 nm and the average diameter was ~9 nm. The spheroid size remained more or less unaltered in comparison to the 15 min sample. As the time was increased to 8 h, morphology of the majority of particles was found to be rodlike with lengths ranging from 35 to 200 nm (average diameter ~9 nm); however, a very small number of rugby balls (length < 30 nm) was also observed (Figure 3). The number of spheroids remained more or less same as in the case of 4 h sample.

Statistical analysis over a spread of TEM images showed a gradual change in morphology depending on the contact time (Figure 4). At 15 min, 95% of the particles were spheroids and only 5% of rugby balls were observed. When the contact time was increased to 4 h, the distribution changed to 25% spheroids, 61% rugby balls, and 14% nanorods. However, at 8 h, the spheroid number remained at 29%, whereas the number of rugby balls reduced to 3% and that of nanorods increased to 68%. Bulk chemical analysis showed that the amount of Pt was more or less same in all the three samples (0.5−0.54 wt %). Dispersion of the nanoparticles was found to be uniform in the micrometer range from SEM-EDAX elemental mapping analysis (data given in the Supporting Information); however, in smaller range, the samples were not uniform; silica particles with only negligible number of Pt nanoparticles were also observed. Distribution of Pt based on TEM images of only those silica particles with Pt encapsulated was calculated to vary within 1−2 nm^3/nm^2 in all the three samples, indicating that the same amount and distribution of Pt led to the formation of various morphologies.

N_2 adsorption isotherms also indicated a change in textural properties depending on the contact times (Figure 5). The mesoporosity of **S1** is retained without any pore blockage as indicated by the sharp rise in the capillary condensation step. However, this was not the case in **S2** and **S3** with much lower capillary condensation showing a reduction in mesoporous nature as well as surface area. This is corroborated by low angle XRD indicating a decreased crystallinity. These observations can be attributed merely to the inherent crystallinities of the samples, however, a contribution from the presence of elongated nanoparticles inside the channels cannot be ruled out.

Most noteworthy observation here is that same amount of platinum adopts different morphologies as the contact time is increased from 15 min to 8 h and the growth of the particles is along the channel direction − raising the question whether any sintering mechanism is involved resulting in elongation of the particles. An in situ variable temperature XRD study on **S1** shows that the

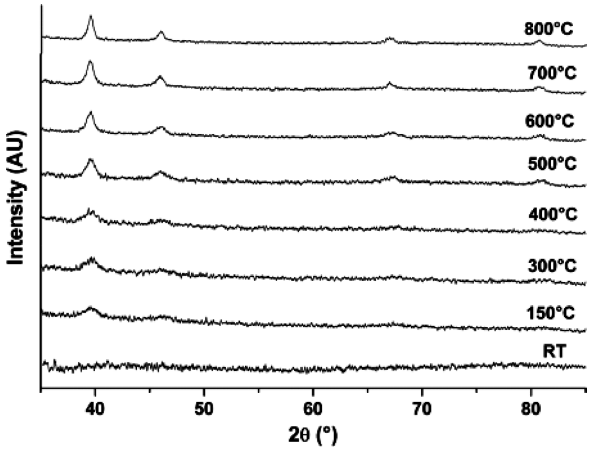

Figure 6. Variable-temperature powder XRD patterns of as synthesized **S1** from 25 to 800 °C.

nanoparticle formation occurs primarily during calcination (Figure 6).

No peaks corresponding to Pt lattice planes were observed in the as-synthesized sample showing that Pt does not exist as metal nanoparticles detectable by XRD. As temperature increases, Pt peaks evolve and increase in intensity showing an increase in size and crystallinity. A similar observation was made by in situ variable temperature solid state UV spectroscopy (see the Supporting Information, Figure 6), which showed the presence of $[PtCl_6]^{2-}$ ligand charge transfer peak around 270 nm in the as synthesized sample which gradually disappeared with increase in temperature.[37] TEM images of the sample heated to 800 °C shows highly sintered particles retaining their spheroid structure but bigger than the pore diameter of the mesochannel (see the Supporting Information, Figure 7). This indicates that the sintering mechanism[38] does not support lateral growth of particles (along the channel direction). TEM images of **S3** heated at 300 °C (see the Supporting Information, Figure 8), at the onset of nanoparticle formation, showed the presence of nanorods indicating that the formation of various morphologies is not related to sintering of nanoparticles. A plausible explanation for the formation of different morphologies is as follows: the Pt ion local concentration, at 15 min, is highly dispersed conducive for the formation of spherical particles on calcination—as in the case of any conventional ion-exchange or impregnation methods. As contact time increases, the local concentration profile of Pt ions is shaped so that it facilitates the formation of progressively elongated particles. This may be due to an aggregation or coalescence of the $[CTA]_2[PtCl_6]$ complex whose structure and nature is yet to be determined, along the axis of the micelle; the polymer template somehow molding the shape and preventing agglomeration perpendicular to the micelle axis. During calcination and consequent reduction, this local concentration profile is retained and the final particle morphology reflects this.

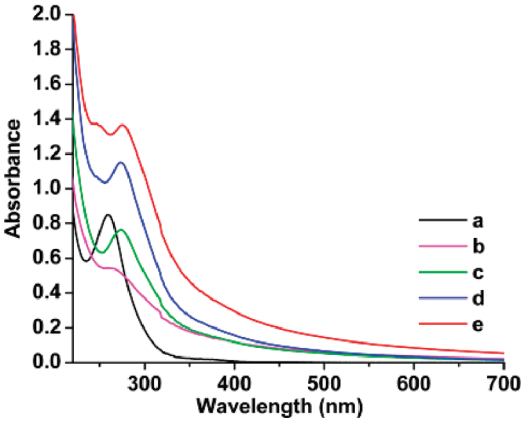

Figure 7. UV−vis spectra of (a) 0.5 mM H_2PtCl_6 and its mixture with 1 wt % P123 and (b) 0.25, (c) 0.5, (d) 1, and (e) 2 mM CTAB.

In other words, the final particle morphology is shaped in the precursor stage. Because the only parameter that was changed during synthesis was the duration for which the metal ion was kept in contact with the modified micelle, the morphology change can be attributed to a local concentration profile variation brought about by precursor aggregation or coalescence along the micelle. At this stage, the nature of the precursor state is not evident. To follow the concentration profile of the precursor with time, the reaction was arrested at particular durations and $NaBH_4$ was employed for reduction of the precursors. These samples were observed by TEM; however, no useful information could be obtained out of it because of agglomerated particles (see the Supporting Information, Figure 9). Because of the limitations set by the nano size scale of the micelles, no concentration profile mapping techniques could be used. However, a series of experiments were carried out by UV−vis spectroscopy and NMR spectroscopy to investigate the state of precursor and its interaction with polymer and surfactant.

UV−vis spectroscopic studies were carried out by changing different parameters to see the effect of contact time as well as CTAB concentration on the chemical environment of platinum. The concentration of CTAB in 1 wt % P123 was progressively increased from 0.25 mM to 2 mM and 0.5 mM H_2PtCl_6 was added to each of these solutions before measuring UV−vis spectra (Figure 7). These spectra were compared with that of pure H_2PtCl_6 in 1 wt % P123, which had a peak at 260 nm attributed to ligand to metal charge transfer.[39,40] We could see a definite shift in this peak position to 285 nm as CTAB concentration increased to 1 mM. This red shift can be attributed to a Coulombic interaction leading to 2:1 ion pairs of the form $[CTA]_2[PtCl_6]$.[32]

This shift was not seen when the precursor was added to unmodified polymer and hence suggesting a stronger interaction of $[PtCl_6]^{2-}$ with the ionic groups of CTAB. However, UV spectra of the H_2PtCl_6 dispersed in polymer

(37) Duff, D. G.; Edwards, P. P.; Johnson, B. F. G. *J. Phys. Chem.* **1995**, *99*, 15934.
(38) Gabaldon, J. P.; Bore, M.; Datye, A. K. *Top. Catal.* **2007**, *44*, 253.
(39) Creighton, J. A.; Eadon, G. *J. Chem. Soc., Faraday Trans.* **1991**, *87*, 3881.
(40) Henglein, A.; Ershov, B. G.; Malow, M. *J. Phys. Chem.* **1995**, *99*, 14129.

surfactant composite micelle did not show any variation with time (Figure 8).

This indicates that there is definitely a change in the chemical environment of Pt immediately on addition to the composite micelle which remains unaltered with time. Hence it is clear that there is an instant dispersion of $[PtCl_6]^{2-}$ because of the electrostatic interaction with CTAB. With time, the environment of $[PtCl_6]^{2-}$ does not change because it is still interacting with CTAB. This important observation gives credence to the possible mechanism for the Pt precursor concentration profile; the formation of $[CTA]_2[PtCl_6]$ complexes inside the polymer micelle which coalesce and aggregate with time. The large time scales in which the morphology change is observed may be due to this slow higher order aggregation.

NMR data also corroborated these observations (see Figure 9). A comparison of the ^{1}H NMR spectra of P123 and P123-CTAB composite micelle showed an overall broadening of the CTAB protons indicating an interaction of CTAB with P123 (see the Supporting Information, Figure 10a&b). The changes occurring to the head (hydrophilic) and tail (hydrophobic) methyl groups were followed to understand the nature of the interaction of CTAB with P123 as well as $[PtCl_6]^{2-}$. When compared to 1 mM CTAB, which is expected to be in micellar form, a mixture of P123 and CTAB shows a low field shift for both the methyl groups indicating their cooperative interaction with P123. On addition of H_2PtCl_6, a sudden drop in concentration of CTAB in solution is observed (~70%), in accordance with the presence of a slight turbidity in the solution (Figure 8). The solubilized portion of the total CTAB concentration still in solution behaves similar to the CTAB−P123 system, showing that it is still interacting with P123.

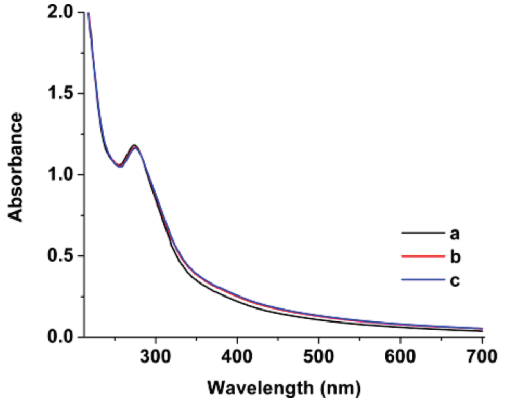

Figure 8. UV−vis spectra of 1 wt % P123, 1 mM CTAB, and 0.5 mM H_2PtCl_6 composite at varying contact times: (a) 15 min, (b) 4 h, and (c) 8 h.

This shows that most of the CTAB molecules now exists in a rigid solid like complex with Pt which give rise to broad lines and are not detected in the spectral window (~8000 Hz) used for the observation of the narrow signals of the molecules in solution. The free CTAB in solution state decreases slightly as contact time increases, indicating more and more CTAB being part of the rigid complex. However, addition of excess H_2PtCl_6 also resulted in an immediate and significant decrease in this CTAB concentration (see the Supporting Information, Figure 11). This shows that there is excess of CTAB not interacting with $[PtCl_6]^{2-}$ in solution and this excess solubilized CTAB becomes part of the rigid CTAB−$[PtCl_6]^{2-}$ complex with time. Further insight into the state of the precursor was sought by ^{1}H self-diffusion studies using PFGNMR (data given in Supporting Information). The CTAB molecules showed only a single self-diffusion coefficient for the 1 mM solution, in CTAB−P123 mixed micelle and also in presence of $[PtCl_6]^{2-}$. The self-diffusion coefficient decreases nearly by an order on formation of mixed micelles. On addition of H_2PtCl_6 to this mixed micelle, the diffusion coefficient of CTAB molecules remaining in the solution was very close to that of CTAB−P123 system. Unfortunately, further study into the nature of precursor structure could not be performed by NMR because of the practical difficulties of simulating the conditions used for the nano particle formation for the measurements.

The fact that we consistently observe the presence of nanoparticles of varying morphology exclusively within the channels of the mesoporous silica and also that the CTAB in solution may not be interacting with $[PtCl_6]^{2-}$ indicates that the rigid complex exists within the

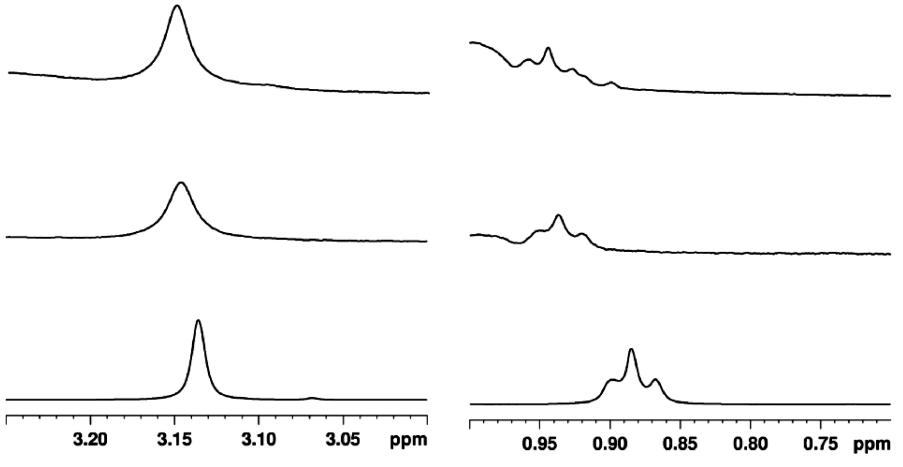

Figure 9. ^{1}H NMR spectra of CTAB (bottom), CTAB-P123 composite (middle) and H_2PtCl_6 added to CTAB-P123 composite (top); left: hydrophilic head methyl group protons and right: hydrophobic tail methyl group protons.

polymer micelle. However, a microphase separation of $[CTA]_2[PtCl_6]$ complex from the P123 micelle can be considered as a possibility. To understand the factors affecting this phenomenon, a mixture of P123, CTAB, and H_2PtCl_6 was ultracentrifuged and the colloid and liquid phases were separated and a qualitative characterization of the phases was attempted by IR spectroscopy (see the Supporting Information, Figure 12). It was observed that the particulate phase was a composite of P123 as well as CTAB, whereas the filtrate was mostly P123 with a reduced amount of CTAB present. This is very much in agreement with NMR results indicating a rigid solid like $[CTA]_2[PtCl_6]$ complex but still interacting with P123. During silica formation, the P123−CTAB−$PtCl_6$ composite micelle as well as free P123 act as templates; the inhomogeneity of the samples with respect to Pt dispersion may have risen from this factor. These extensive studies have shown that the formation of nanoparticles with different morphologies occurs with different contact times, which may be due to varying extents of agglomeration of a rigid CTAB−$PtCl_6$ complex precursor. This also supports large time scales in which morphology variation is observed.

Conclusion

Different morphologies of platinum nanoparticles, viz. spheroids, nanorugby balls and nanorods could be isolated exclusively inside channels of mesoporous compounds by varying synthetic parameters in situ. Usually, pore filling of mesoporous compounds with high concentrations of noble metal precursors is employed for nanorod fabrication by template methods. We have demonstrated that at very low concentrations, nanoparticle morphology can be controlled and fine-tuned by easily varying extent to which $[CTA]_2[PtCl_6]$ complex precursor is allowed to agglomerate in the composite micelle template prior to the formation of the siliceous mesochannels and these modifications could be achieved with the same concentration of platinum. These factors are crucial in nanoparticle synthesis especially for catalysis, because highly dispersed low weight percentage of noble metals supported on oxides are ideal materials as heterogeneous catalysts.

Acknowledgment. A.K.P. acknowledges CSIR, New Delhi, India, for a fellowship, and R.P.H., through Prof. Lennart Bergström, Stockholm University, thanks the Swedish Research Council (VR) for funding. We thank RSIC, IIT Mumbai, India, for ICP analysis and Dr. G. Kumaraswamy and Dr. Amol Kulkarni, NCL, for useful discussions.

Supporting Information Available: Experimental details, more HRTEM images, N_2 adsorption data, more NMR spectra, NMR diffusion data, IR and solid-state UV spectra (PDF). This material is available free of charge via the Internet at http://pubs.acs.org.